Asteroid Magnetization from the Early Solar Wind

Atma Anand^{1★}, Jonathan Carroll-Nellenback¹, Eric G. Blackman¹, John A. Tarduno^{1,2}

¹Department of Physics and Astronomy, University of Rochester, Rochester NY 14627

May 2021

ABSTRACT

Magnetic fields provide an important probe of the thermal, material, and structural history of planetary and sub-planetary bodies. Core dynamos are a potential source of magnetic field amplification in differentiated bodies, but evidence of magnetization in undifferentiated bodies requires a different mechanism. Here we study stellar wind-induced magnetization (WIM) of an initially unmagnetized body using analytic theory and numerical simulations, employing the resistive MHD AstroBEAR adaptive mesh refinement (AMR) multiphysics code. We obtain a broadly applicable scaling relation for the peak magnetization achieved once a wind advects, piles-up, and drapes a body with magnetic field, reaching a quasi-steady state. We find that the dayside magnetic field for a sufficiently conductive body saturates when it balances the sum of incoming solar wind ram, magnetic, and thermal pressures. Stronger amplification results from pileup by denser and faster winds. Careful quantification of numerical diffusivity is required for accurately interpreting the peak magnetic field strength from simulations, and corroborating with theory. As specifically applied to the Solar System, we find that early solar wind-induced magnetization is a viable explanation for observed paleointensities in some undifferentiated bodies. This magnetism mechanism may also be applicable for other Solar System bodies, including metal-rich bodies to be visited in future space missions such as the asteroid (16) Psyche.

Key words: magnetic fields; planet–star interactions; asteroids – Sun: evolution – meteors; meteoroids; stars: winds, outflows;

1 INTRODUCTION

The terrestrial planets Mercury, Earth, and Mars have all at some point likely hosted internal convective core dynamos that generate planetary magnetic fields from within (e.g. Johnson et al. 2015, 2020b; Bono et al. 2019; Tarduno et al. 2015, 2020). Core dynamos are possible only for objects which have a sufficient energy source and have incurred sufficient differentiation to sustain a liquid metal core. However, it is unclear whether sufficient differentiation to generate a liquid core has occurred in smaller Solar system bodies like asteroids. If they are magnetized but undifferentiated, then the their magnetic fields would have to be externally supplied.

Information about early asteroids - especially those destroyed in the collisions ubiquitous to development of the Solar System - comes from the study of meteorites. In general, paleofield strength data from paleomagnetic measurements can be used to detect the ambient magnetic field during the formation of magnetic minerals in the studied meteorites. These potential field sources include those of the protoplanetary disk nebula (Nagata 1979), solar wind, or dynamos in the parent bodies of meteorite parent bodies (Collinson et al. 1994).

Some achrondite meteorites are clearly from highly differentiated parent bodies, and paleomagnetic measurements from multiple groups have revealed evidence for strong parent body paleofields. For example, pallasites—meteorites that are composed of olivine and FeNi metals—are clearly derived from a highly differentiated asteroid.

* aanand6@ur.rochester.edu

High paleofields from the main group pallasites were first detected by magnetic studies of olivine bearing magnetic inclusions; these data indicated the presence of a core dynamo after an impact that formed the characteristic pallasite textures (Tarduno et al. 2012). Dynamo sourced paleofields were also reported from magnetic studies of nanostructures in the FeNi metal (Bryson et al. 2014a,b). In contrast, meteorites from undifferentiated parent bodies with magnetic minerals formed after dispersal of the protoplanetary disk nebula, are expected to record only magnetic fields supplied by the solar wind.

In this context, an important case is the Allende meteorite - a CV (Vigrano type) carbonaceous chondrite, long though to be a classic example of a primitive meteorite from an undifferentiated body (Scott & Krot 2014). Strong apparent magnetizations were known for Allende from classic studies (e.g. Nagata 1979) but only more recently were these interpreted as requiring paleofields 10's of μ T, de facto evidence for a core dynamo, and differentiation of the CV type parent asteroid (Carporzen et al. 2011; Weiss & Elkins-Tanton 2013; Elkins-Tanton et al. 2011). But this interpretation of the magnetic data has been the only evidence of differentiation. The 26 Al content seems insufficient to produce the heat needed for melting required in the differentiation of the parent body (Scott & Krot 2014; Nagashima et al. 2017, 2018), and there is no evidence for differentiated components in meteorite collections.

The question of differentiation of the CV parent body was reinvestigated by Tarduno et al. (2016) and O'Brien & Tarduno (2016) who discovered that Allende's magnetization was a consequence of magnetic interactions associated with its magnetic mineralogy - es-

²Department of Earth and Environmental Sciences, University of Rochester, Rochester NY 14627

pecially pyrrhotite - rather than a reliable paleofield measurement. Allende's magnetization is thus not useful for determining early ambient Solar System magnetic fields. While this solved the Allende magnetization puzzle, returning the CV parent body to its proper place amongst undifferentiated asteroids, the question of what early ambient field strengths could arise has remained.

Fortunately, other CV as well as CM (Mighei-type) carbonaceous chondrites meteorites, have more reliable magnetic recorders (i.e., magnetite) that can preserve useful indicators and constrain early Solar System magnetic fields. Tarduno et al. (2017) proposed solar wind induced magnetization (WIM) as a plausible mechanism to explain the magnetization of these meteorite parent bodies, and outlined theory supporting this interpretation. Oran et al. (2018) produced a series of magnetohydrodynamic (MHD) simulations and argued that the solar wind was an insufficient source. However, in O'Brien et al. (2020) we show that with early solar wind parameters within an accepted range of observations and current theory (Johnstone et al. 2015; Blackman & Owen 2016; Wood et al. 2005; Tarduno et al. 2014), a solar system object at ~ 2 AU having a sufficiently conductive parent body or a thin conductive shell may pile up sufficient magnetic field strength to explain the paleointensity data from CV, and CM meteorites with reliable magnetic recorders.

In this manuscript we carry out a more general numerical study of small body magnetization by a stellar wind and obtain broadly applicable scaling relations. These are especially relevant for early Solar System bodies already known by meteorites, or to be be visited by future space missions such as that to investigate (16) Psyche (Elkins-Tanton et al. 2020). In §2, we discuss our numerical model and methods used, in §3 we provide and discuss theoretical estimates, in §4 we showcase our results, in §5 we interpret our findings and identify directions for future work, and in §6 we conclude our results.

2 MODEL AND METHODS

Using the adaptive mesh-refinement (AMR) code, AstroBEAR (Cunningham et al. 2009; Carroll-Nellenback et al. 2013), we simulate a magnetized solar wind overrunning an asteroid. For different runs we use different resistivity values and profiles for the asteroid, and each run was evolved to a steady state.

To carry out our simulations, we need a model for the early solar wind, the resistivity profile of the asteroid, initial and boundary conditions, and criteria for a sufficiently steady-state. We can then compare the theoretical framework of §3 to the numerical results.

2.1 Solar wind and grid setup

The early solar wind is thought to have a higher density and magnetic field strength than that of the present day, based on observations and modeling of young stars similar to the Sun (Wood et al. 2005; Tarduno et al. 2014; Johnstone et al. 2015; Blackman & Owen 2016). We give the young stellar wind an ion density of 1000 cm^{-3} or 300 cm^{-3} , a temperature of 5×10^5 K, a velocity of 500 kms^{-1} (in x), and a magnetic field of 100 nT (in the y direction) perpendicular to the flow. The above values correspond to a stellar wind Mach number of 4.74, the ratio of thermal to magnetic pressure β of 3.47 or 1.04, and an Alfvénic Mach number of 8 or 4.38. We use an separate wind having parameters of 300 cm^{-3} , $150 \times 10^3 \text{ K}$, 500 km s^{-1} , and 14 nT to test the effects of our grid (see Table 1 for more details). The mean mass of solar wind particles in all cases is 0.623 amu, considering that Hydrogen, and Helium atoms will be ionized.

The asteroid is modeled as a solid boundary of radius 500

km but allowed to have different interior resistivity structures. The solution results can be rescaled to arbitrary asteroid radii, provided that the asteroid radius exceeds the ion Larmor radius. The wind density, temperature, velocity, and magnetization can also be rescaled provided that the same plasma β and Mach number are used.

We initialize the grid with the aforementioned stellar wind conditions, but make modifications in the vicinity of the asteroid as described below. The wind is continuously injected from the left (-x) boundary during the simulation. The y and z simulation boundaries are extrapolated as is the right boundary (+x), allowing for the wind, and the wake behind the asteroid, to flow through the boundary. The boundaries are sufficiently far away such that the wake behind the asteroid does not pass through them - and the solar wind remains unperturbed (plane parallel).

We use a base resolution of 64x64x64 with 4 additional levels of adaptive mesh refinement (AMR) around the asteroid, allowing resolution of the asteroid's diameter with 128 zones. We performed a resolution study, comparing runs from 3 to 5 AMR levels which confirmed that the simulated field is sufficiently resolved at the asteroid boundary, and a convergence study which confirmed that the field reached steady state for all models (details are excluded from this study).

2.2 Equations solved

Simulations were conducted using AstroBEAR ¹ (Cunningham et al. 2009; Carroll-Nellenback et al. 2013), a publicly available, massively parallelized, adaptive mesh refinement (AMR) code that contains a variety of multi-physics solvers (i.e. self-gravity, magnetic resistivity, radiative transport, ionization dynamics, heat conduction, etc). The physical mass, momentum and energy equations solved are

$$\frac{\partial \rho}{\partial t} + \nabla \cdot (\rho v) = 0 \tag{1}$$

$$\frac{\partial \rho \mathbf{v}}{\partial t} + \nabla \cdot (\rho \mathbf{v} \mathbf{v} - \mathbf{B} \mathbf{B}) = -\nabla P^* \tag{2}$$

$$\frac{\partial E}{\partial t} + \nabla \cdot \left[(E + P^*) \boldsymbol{v} - \boldsymbol{B} (\boldsymbol{B} \cdot \boldsymbol{v}) \right] = -\nabla \cdot (\eta \boldsymbol{J} \times \boldsymbol{B})$$
 (3)

$$\frac{\partial \boldsymbol{B}}{\partial t} - \nabla \times (\boldsymbol{v} \times \boldsymbol{B}) = -\nabla \times (\eta \boldsymbol{J}) \tag{4}$$

where ρ is the mass density, \boldsymbol{v} is the velocity, $P^* = P + \frac{B^2}{2}$ where P is the gas pressure, \boldsymbol{B} is the magnetic field, the total energy $E = \frac{P}{\gamma - 1} + \frac{1}{2}\rho v^2 + \frac{B^2}{2}$ and the magnetic diffusivity is given by η . We set $\gamma = \frac{5}{3}$ and use the non-relativistic approximation $\boldsymbol{J} = \boldsymbol{\nabla} \times \boldsymbol{B}$.

In practice, we found it necessary to add a small amount of explicit numerical diffusion throughout the simulation domain (similar to that used in higher order schemes to damp oscillations at regions of flow convergence) to smooth over the discrete representation of the asteroid surface on our Cartesian grid. This was accomplished by adding $-\alpha \nabla U$ to the corresponding fluxes for the conserved fluid variables $U = [\rho, \rho v, E]$.

$$\frac{\partial U}{\partial t} = \nabla \cdot (\alpha \nabla U) \tag{5}$$

https://astrobear.pas.rochester.edu/

where α was chosen to be as small as possible. In addition the magnetic field was updated in a divergence conserving manner using

$$\frac{\partial \mathbf{B}}{\partial t} = -\nabla \times (\alpha \nabla \times \mathbf{B}) = -\nabla \times (\alpha \mathbf{J}), \tag{6}$$

so that the right side acted like a source of additional magnetic diffusion throughout the simulation domain. As the simulation approached steady state, the α was ramped down to values small enough to smooth out gradients only on the finest grid scale - and to levels where the additional diffusion was comparable to the intrinsic numerical diffusion. This additional diffusion was only applied outside the asteroid.

2.3 Initial velocity and magnetic fields

Asteroids could potentially have outer layers of higher conductivity or atmospheres, particular in the young Solar System (Brownlee 2005; O'Brien et al. 2020), and so a number of our runs focus on asteroid surfaces with low resistivity so that the initial magnetic field takes a long time to diffuse through and reach a steady state. Hence, we initialize the magnetic field to exclude the asteroid and a couple of zones outside it. To enforce $\nabla \cdot \mathbf{B} = 0$, we solve for the magnetic vector potential \mathbf{A} (where $\mathbf{B} = \nabla \times \mathbf{A}$) of a magnetically shielded sphere with no field inside and a fixed \mathbf{B}_0 field at infinity. We have

$$\mathbf{A} = \begin{cases} B_0 \left(1 - \frac{r_e^3}{r^3} \right) \hat{\mathbf{B}} \times \mathbf{r} & ; r > r_e \\ 0 & ; r \le r_e \end{cases}$$
 (7)

where B_0 is taken to be that of the solar wind, r_e is the exclusion radius of the magnetic field, r is the position vector from the center of the asteroid, and $\hat{\mathbf{B}}$ is the direction of the magnetic field. The assumed incompressible wind velocity vector is chosen to be proportional to the magnetic field. That is, the curl of Eqn. 7 was taken, transposed, and scaled with a peak value equal to that of the solar wind velocity. This also makes it divergence free, as one would expect for an incompressible flow around a spherical obstruction.

Fig. 1 shows a slice in the xy midplane of the solar wind velocity, electrical resistivity, and ambient magnetic field setup for the initial (t = 0) frame. The wind velocity is in the x direction, carrying magnetic field in the y direction. Note the exclusion of the field and wind from the asteroid, and the similar setup for the wind velocity and magnetic field.

2.4 Asteroid boundary conditions

The asteroid is incorporated into the simulation box as an internal partially absorbing boundary similar to Jia et al. (2015). When the flow is into the boundary, the flow density and internal energy are extrapolated and the flow velocity is multiplied by an absorption factor to allow for control of how much mass, momentum, and energy is absorbed. When this factor is 1, the boundary fully absorbs the incoming mass, momentum, and energy. When the factor is -1, the boundary reflects, allowing no mass, or energy to pass through. We find that the value of the absorption factor makes observable differences in the final steady state solution – particularly for high magnetic Reynolds' number (R_M) cases, with absorbing boundaries having more field pileup.

When the flow is away from the boundary, the boundary acts as a low density and pressure region, and allows some material to be drawn out through it. On the night side, this extra material helps to limit the Alfvén speeds that could otherwise be produced

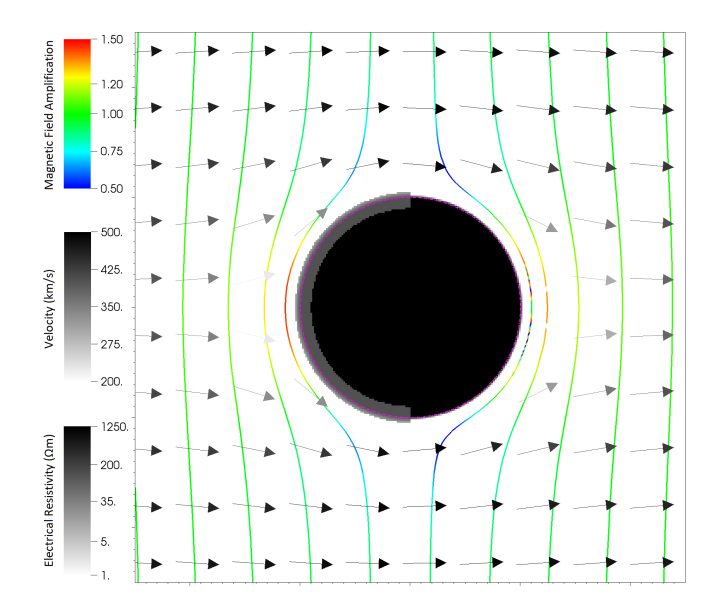


Figure 1. Initial values of the magnetic field amplification (lines), and velocity (arrows) as per Eqn. 7, and comet-like resistivity structure in the xy midplane. The resistivity of the ambient is negligible. We also use uniform (fully black colored body) and shell-like resistivity (grey shell extends to both hemispheres) profiles. There is an exponential resistivity smoothing of 3 zones merging into the ambient. The particle density inside the body is fixed to be low (~ 10 ions), while the ambient wind has density of $1000~\rm{cm}^{-3}$ and field of $100~\rm{nT}$.

by the diffusive flux of magnetic fields through this boundary into what would otherwise be a very low density environment. The initial asteroid density is also chosen high enough to avoid extremely high Alfvén speeds behind the asteroid, but much lower than the ambient wind so as to not be a significant source of particles.

The asteroid density is slowly ramped down over the course of the simulations to limit its influence on the exterior magnetic structure and facilitate a steady state. In all cases, there is no advection of magnetic fields across the boundary or within the asteroid, only magnetic diffusion.

2.5 Asteroid interior resistivity

We model our asteroid as a body with radius $R = 500 \,\mathrm{km}$ and three different resistivity profiles.

- (i) **Uniform:** In this case, the resistivity is constant with radius. This is the simplest case and can be readily extended to a family of models with different resistivities, all other conditions being the same. This case corresponds to cool, small asteroids or moons, that are low in volatiles.
- (ii) **Conductive Outer Shell:** For this case the outer 10% shell is 10 times more conductive than the body. This allows the field to pile up more effectively at the outside boundary of the shell. The shell could correspond to a surface layer of enhanced conductivity within the body itself, or an atmospheric layer above the body. Venus, with its dense atmosphere would be an extreme example of the latter.
- (iii) **Cometary:** In this case the outer 10% shell on the dayside has a higher conductivity compared to that on the night side and body of the asteroid, the latter two of which are equal (see Fig. 1). This case is similar the interaction of comets with the solar wind, which leads to volatiles escaping and forming a conductive layer on the dayside. Such an interaction may be particulally relevant for the early solar

wind (Brownlee 2005; O'Brien et al. 2020). Fig. 1 exemplifies this case for a body of $R_M = 500$ and dayside shell of $R_M = 5{,}000$.

The total size of the object is the same in all cases. The shell or cometary layer is included in the simulation at the expense of zones in the body.

For the cases with uniform diffusivity, η , the magnetic Reynolds number $R_M \equiv \frac{2v_w R}{\eta}$ and can be thought of as the ratio of advective flux around the asteroid $(v_w B)$ to diffusive flux through the asteroid $\left(\frac{\eta B}{2R}\right)$. For models with $R_M \lesssim 1$, magnetic fields readily diffuse through the asteroid, while for models with $R_M >> 1$, magnetic fields pile up on the upwind side faster than they can diffuse through the body. The latter leads to an preferential increase of magnetic pressure over thermal pressure because material can escape along field lines parallel to the body, leaving the magnetic pressure to balance and divert the the solar wind around the asteroid. For the cases with non-uniform diffusivity, we compute an the magnetic Reynolds using an effective diffusivity $\bar{\eta}$ which we define as the inverse of the current weighted conductivity

$$\frac{1}{\bar{\eta}} = \bar{\sigma} = \frac{\int \sigma |\nabla \times \mathbf{B}| \, dV}{\int |\nabla \times \mathbf{B}| \, dV} = \frac{\int \frac{1}{\eta} |\nabla \times \mathbf{B}| \, dV}{\int |\nabla \times \mathbf{B}| \, dV}$$
(8)

For our choice of solar wind speed $v_w = 500 \,\mathrm{km \ s^{-1}}$ and asteroid radius of 500 km, the critical magnetic diffusivity η_c for which $R_M = 1$ is 5×10^{11} m²s⁻¹, corresponding to an electrical resistivity $\approx 6.3 \times 10^5 \,\Omega \text{m}.$

For the asteroid electrical resistivity (ρ_e) we use values based on the heating curve of Sample 1 of Allende (heated at 3°C hr⁻¹) in Duba & Boland (1984) at 300°C, consistent with not having a differentiated interior. This gives $\rho_e \sim 1250 \,\Omega m$, and a magnetic Reynolds number, $R_M \approx 500$.

2.6 Steady state criteria

Wherever possible, all simulations were run to a maximum of ~ 72 seconds or a suitable fraction of the diffusion time periods. The steady state was verified by verifying that the rate of change of maximum field drops to a negligible value in successive output frames.

3 LIMITS FROM ANALYTIC THEORY

3.1 Limits on magnetic amplification due to asteroid diffusivity

If we consider a steady state solution in 1D, the induction equation

$$\frac{d}{dx}\left(vB - \eta \frac{dB}{dx}\right) = 0\tag{9}$$

which states that the combined advective diffusive flux of the magnetic field must be constant and equal to the incoming advective flux

$$vB - \eta \frac{\mathrm{d}B}{\mathrm{d}x} = v_w B_0. \tag{10}$$

Within any slab of width 2R interior to an asteroid, v = 0 and equation (10) becomes

$$\eta \frac{\mathrm{d}B}{\mathrm{d}x} = v_w B_0 \tag{11}$$

If we further assume that any fields which diffuse through the asteroid from left to right are quickly removed, so that the field at the right edge of the slab ≈ 0 , the field at the inflowing edge needed to provide a sufficient gradient to diffuse the field through the body as quickly as it is being advected in can be estimated as

$$B_{\text{max}} = v_w B_0 \int_0^{2R} \frac{\mathrm{d}x}{\eta} = B_0 \frac{2v_w R}{\bar{\eta}} = B_0 R_M, \tag{12}$$

and the expected amplification factor

$$A \equiv \frac{B_{\text{max}}}{B_0} = R_M \tag{13}$$

where
$$\bar{\eta} = \left(\frac{\int \frac{1}{\eta} dx}{\int dx}\right)^{-1}$$
.

So in 1D, the field can diffuse through the slab as quickly as it piles up, once the amplification factor has reached R_M . This provides a conceptual upper limit on the amplification of the magnetic field as it piles up on the upwind side of the asteroid.

3.2 Limits on amplification due to diffusion around the asteroid

In 3D, the magnetic field can diffuse around the asteroid as well as through - so if the diffusion of the wind material (turbulent, numerical, microphysical) is large enough, this can also limit the amplification to the corresponding Reynolds number.

$$A = R_{M\alpha} \equiv \frac{v_W R}{\alpha} \tag{14}$$

Here α is the manually adjustable numerical diffusion present in the code, and is mostly dependent on the grid size.

3.3 Limits on amplification due to pressure confinement

We now allow for transverse motion perpendicular to the wind flow away from the \hat{x} axis. For the steady state wind flow exactly along the \hat{x} axis, we have from symmetry $v_y = v_z = B_x = B_z = 0$. We can therefore write the mass continuity equation as

$$\frac{\partial}{\partial x} \left[\rho v_x \right] = -\rho \left(\frac{\partial v_y}{\partial y} + \frac{\partial v_z}{\partial z} \right). \tag{15}$$
Transverse mass loss

This is like the 1D case - but with an extra mass loss term involving the divergence of the transverse velocities. Material can now be deflected along field lines in the y direction or perpendicular to the field lines in the z directions.

Correspondingly, the \hat{x} component of the momentum equation

$$\frac{\partial}{\partial x} \left[\rho v_x^2 + P + \frac{1}{2} B_y^2 \right] = \underbrace{B_y \frac{\partial B_x}{\partial y}}_{\text{Magnetic tension}} \underbrace{-\rho v_x \left(\frac{\partial v_y}{\partial y} + \frac{\partial v_z}{\partial z} \right)}_{\text{Transverse mass loss}}, \quad (16)$$

which also has a corresponding transverse mass loss term acting to reduce the momentum flux approaching the body, along with a magnetic tension term that increases the momentum flux.

The induction equation also has an additional term related to the

transverse deflection of magnetic fields - but only in the \hat{z} direction.

$$\frac{\partial}{\partial x} \left[v_x B_y \right] = -B_y \frac{\partial v_z}{\partial z} \qquad . \tag{17}$$

Field line deflection in \hat{z} only

These equations show that both mass, and the corresponding momentum and energy, can be redirected both along field lines (in y) and perpendicular to them (in z), while the magnetic field can only be redirected in the z direction.

We can integrate the momentum equation towards the asteroid boundary to arrive at

$$\rho_{b}v_{b}^{2} + P_{b} + \frac{1}{2}B_{b}^{2} = \rho_{0}v_{0}^{2} + P_{0} + \frac{1}{2}B_{0}^{2} + \int \left[B_{y} \frac{\partial B_{x}}{\partial y} - \rho v_{x} \left(\frac{\partial v_{y}}{\partial y} + \frac{\partial v_{z}}{\partial z} \right) \right] dx,$$
(18)

where ρ_b , v_b , P_b , and B_b are the density, x velocity, thermal pressure, and y component of the magnetic field at the boundary with the asteroid and variabiles with subscript "0" are the corresponding values of the wind.

If we ignore the integral which involves the mass/field deflection and magnetic tension terms, we can rewrite Equation (18) in terms of the magnetic amplification $A \equiv \frac{B_b}{B_0}$, incoming mach number M. and plasma β

$$\left(1 - \frac{P_b}{P_0}\right) + \gamma M^2 \left(1 - A^{-1}\right) + \frac{1}{\beta} \left(1 - A^2\right) = 0 \tag{19}$$

If we also assume that the movement of material along the field lines reduces the thermal pressure of the material at the asteroid surface so that $P_b \approx P_0$, and assume A >> 1, then Equation (19) simplifies to

$$\gamma M^2 - \frac{A^2}{\beta} = 0 \to A = M\sqrt{\gamma\beta}. \tag{20}$$

This is equivalent to balancing magnetic pressure at the asteroid boundary with the incoming ram pressure of the wind and would be an upper limit to the amplification when all other terms except magnetic tension are included. Of all the terms that we have dropped, only the magnetic tension term could increase the amplification beyond this value.

Combining the ram pressure limit with the diffusion limits (both through and around the asteroid), we then predict the magnetic field amplification to be

$$A \lesssim \max \left[1, \min\left(M\sqrt{\gamma\beta}, R_M, R_{M\alpha}\right)\right]$$
 (21)

This estimate is based on the underlying physics, but in practice we must carefully consider the influence of numerical resolution and numerical diffusion when corroborating Equation (21) with what simulations actually show. We address this further in §5.1.

4 RESULTS

We carried out a suite of runs exploring the parameter space indicated in Table 1. Fig. 2 shows a plot of amplification vs magnetic Reynolds' number for all cases. Fig. 3 shows the midplane slice of magnetic field, density, and velocity of a select few cases, while Fig. 5 shows the 3D field distribution. The O and X type reconnection regions on the night side of the asteroid in Fig. 3 are particularly notable. The

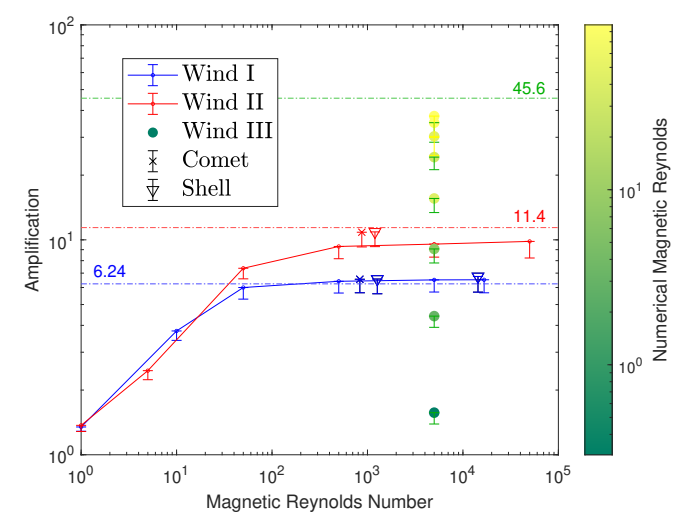


Figure 2. The maximum steady state magnetic amplification vs magnetic Reynolds number for simulations based on three different solar wind models (see Table 1). Wind I: Ion density: $300~{\rm cm}^{-3}$, $500\times10^3~{\rm K}$, $500~{\rm km\,s}^{-1}$, $M\sqrt{\gamma\beta}=6.24$; Wind II: Ion density: $1000~{\rm cm}^{-3}$, $500\times10^3~{\rm K}$, $500~{\rm km\,s}^{-1}$, $M\sqrt{\gamma\beta}=11.4$; Wind III: Ion density: $300~{\rm cm}^{-3}$, $150\times10^3~{\rm K}$, $500~{\rm km\,s}^{-1}$, $M\sqrt{\gamma\beta}=45.6$. Solid curves show constant resistivity profiles having different resistive magnetic Reynolds numbers (R_M) but the same numerical magnetic Reynolds number ($R_{M\alpha}\sim44$). Filled circles show the high $M\sqrt{\gamma\beta}$ case with fill color representing the value of $R_{M\alpha}$. Crosses show shell, and down triangles cometary cases. Dotted lines show theoretical amplification for a given wind from Equation (20). High values of the error bars correspond to the global maxima at the dayside of the body directly perpendicular to the wind, while the low values are the L16 norm over a R/2 (250 km) region around it.

insights we gain from these simulations are summarized for different cases.

4.1 Summary of runs

Table 1 lists our runs and their parameters along with the peak measured field amplification, and the theoretically predicted value from Equation (21).

The amplification column refers to the peak magnetic field amplification, typically at the cell just outside the asteroid (including any outer shell layer), and directly facing the incident wind. There are other ways of computing the amplification, for example the L^n norm where $n \geq 2$. In Fig. 2, we add error bars to reflect this.

The theory column of the table lists the predicted amplification from a balance of the solar wind ram pressure with the magnetic field pressure, ignoring thermal pressure, provided we are above a threshold of conductive and numerical Magnetic Reynolds's number $(R_M \text{ and } R_{M\,\alpha})$ as per Eqn. 21. This somewhat overpredicts the magnetic amplification for cases with higher β (denser wind, in red in Figures), suggesting that thermal pressure contributes to the total pressure, thereby reducing the magnetic pressure needed to balance the ram pressure.

We computationally demonstrate that early solar wind conditions could have caused sufficient pileup to induce the NRM observed in some carbonaceous chondrite meteorites (O'Brien et al. 2020). We found pileup to be close to our theoretical estimate of $M\sqrt{\gamma\beta}$, with the dependence on β being generally slightly weaker, as thermal pressure also contributes to the pressure equilibrium) for sufficiently conductive asteroid surfaces (see Fig. 2). This field pileup saturates at a threshold conductivity above which the magnetic and

Table 1. Summary of Simulations (see text for description of quantities listed)

		Asteroid			Theoretical	Simulated**
		Structure	$R_{\mathbf{M}}^{\dagger}$	$R_{M\alpha}$	Amplification	Amplification
Wind I		Shell	1268	43.71	6.24	6.57
Field (nT)	100	Shell	14382	43.71	6.24	6.75
Temperature (K)	500×10^{3}	Comet	832	43.71	6.24	6.55
Ion density (cm ⁻³)	300	Fixed	1	43.71	1.00	1.35
Velocity (km s ⁻¹)	500	Fixed	10	43.71	6.24	3.77
Mach	4.74	Fixed	50	43.71	6.24	6.00
Beta	1.04	Fixed	500	43.71	6.24	6.41
$M\sqrt{\gamma\beta}$	6.24	Fixed	5000	43.71	6.24	6.51
		Fixed	16667	43.71	6.24	6.52
Wind II		Shell	1198	43.71	11.40	10.89
Field (nT)	100	Comet	872	43.71	11.40	10.85
Temperature (K)	500×10^{3}	Fixed	1	43.71	1.00	1.37
Ion density (cm ⁻³)	1000	Fixed	5	43.71	5.00	2.46
Velocity (km s ⁻¹)	500	Fixed	50	43.71	11.40	7.37
Mach	4.74	Fixed	500	43.71	11.40	9.31
Beta	3.47	Fixed	5000	43.71	11.40	9.55
$M\sqrt{\gammaeta}$	11.40	Fixed	50000	43.71	11.40	9.83
Wind III		Fixed*	5000	87.43	45.60	37.64
Field (nT)	14	Fixed	5000	87.43	45.60	35.08
Temperature (K)	150×10^{3}	Fixed	5000	43.71	43.71	15.58
Ion density (cm ⁻³)	300	Fixed*	5000	43.71	43.71	30.29
Velocity (km s ^{−1})	500	Fixed	5000	30.60	30.60	24.26
Mach	8.65	Fixed	5000	7.65	7.65	9.07
Beta	16.66	Fixed	5000	3.06	3.06	4.42
$M\sqrt{\gamma\beta}$	45.60	Fixed	5000	0.31	1.00	1.57

^{*}Wind III Italicized cases have double grid resolution.

thermal pressure balance the incoming solar wind ram pressure. The timescale to reach the steady state is proportional to a body-shell averaged diffusion timescale.

We find that both the value of the effective conductivity and whether the conductivity is uniform or dominated in a shell both influence the amount of magnetic field pileup. Profiles having an outer conductive 10% shell, as in our cometary and shell models, have higher pileups than cases with same effective conductivity distributed uniformly. However, this field is at the outer boundary of the shell. If this shell represents an atmosphere rather than a body surface layer, turbulent mixing of atmospheric layers would be required for the field reach the main body.

4.2 Constant profile cases

Most of our simulations in Table 1 use a constant resistivity profile. As Fig. 2 shows, the simulated amplification increases almost linearly with R_M , and then asymptotically approaches the theoretical value from Equation (20). The vertical points of different shades of green in the figure show how $R_{M\alpha}$ affects the amplification for a wind with very high β . There, for a fixed R_M , as $R_{M\alpha}$ increases the saturation value again approaches Equation (20) and validates Equation (21).

Figure 3 shows the steady state magnetic amplification, density, and velocity for the denser (1000cm⁻³) wind for R_M = 5×10^4 , 5000, 500, and 5. As expected, the density, and magnetic field pileup increase with the magnetic Reynolds number while the wind velocity remains nearly the same. The lightening in shade on the night side is indicative of the rarefaction there. In general, the mass pileup is much smaller than the field pileup as particles can easily leave in directions parallel to the field and perpendicular to the incoming wind near the body.

Fig. 4, shows a 3D model² of the final field configuration for the constant resistivity profile case with $R_M = 5,000$.

4.3 Shell case

In this case the outer 10% of the shell in radius is 10 times more conductive than the main body. We ran 3 distinct cases of this kind: two with an asteroid body resistivity of $1250 \Omega m$ or 0.2% of the critical resistivity (see §2.5 for definition) but different wind models; and a 10x more conductive case for the 300cm⁻³ wind value. These cases are listed in the first three rows of Table 1. These cases correspond physically to a body with a thick outer conducting shell or atmosphere. In principle, we could further reduce the conductive layer thickness down to the resolution of the grid ($\sim 1.6\%$ of asteroid).

Fig. 3, (d) top right panel, and Fig. 5 (a) top panels show the steady state frame for the shell case for the denser wind. We find the peak amplification of this case (and the cometary case discussed below) to be higher than all constant profile cases, irrespective of R_M , even though the conducting shell itself has a $R_M = 5{,}000$. But the field distribution in Fig. 3 (top-right panel) shows that the peak is more localized within the shell as compared to its broader distribution for the constant profile cases. From the RHS term in Equation (4) and the tension term in Equation (18), we do expect a sharper gradient and higher field inside the shell.

 $^{^{\}dagger}$ R_{M} values for Shell and Comet cases are weight averaged over current.

^{**} Values represent the peak field of all grid cells. See Fig. 2 for error bars.

² Link: https://skfb.ly/o6sKt

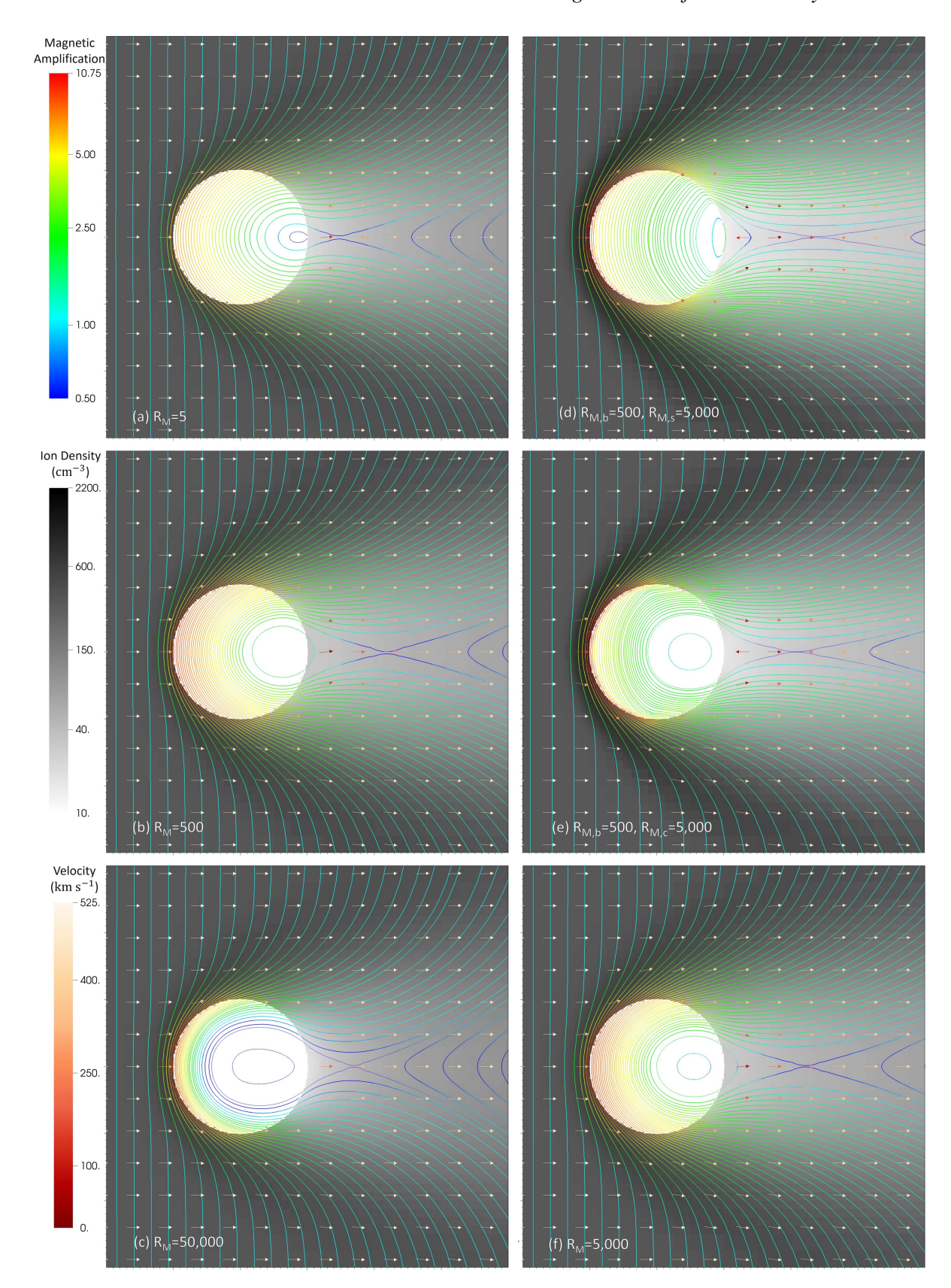


Figure 3. Steady state Magnetic amplification, particle density, and velocity in the xy mid-plane for select cases with $T_w = 500 \times 10^3 K$, $\rho_{i,w} = 1000 \text{cm}^{-3}$, $v_w = 500 kms^{-1}$. The velocity scale is linear while others are logscale. Left column panels: show progression in uniform resistivity cases with no shell layer, (a) Top: $R_M = 5$; (b) Middle: $R_M = 500$; (c) Bottom: $R_M = 50,000$. Right column panels: (see also Fig. 5) (d) Top: Body with $R_M = 500,10\%$ full outer shell $R_M = 5,000$; (e) Middle: Body with $R_M = 500,10\%$ Cometary dayside shell $R_M = 5,000$; (f) Bottom: Constant resistivity profile with $R_M = 5,000$.

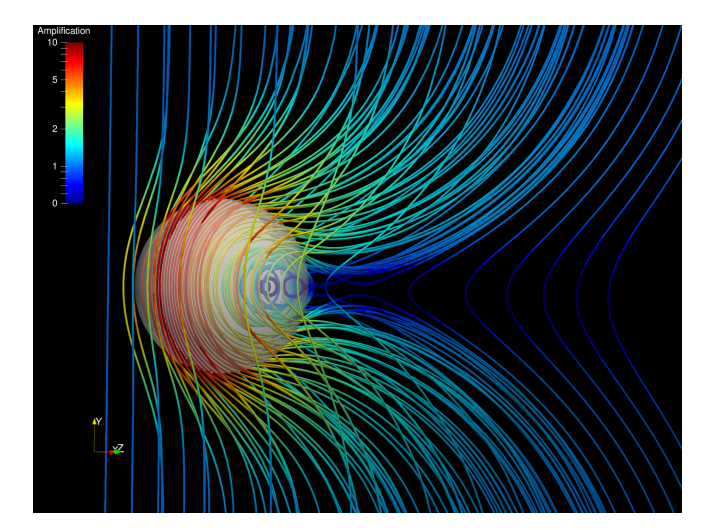


Figure 4. (Interactive figure) Steady state view of magnetic field lines draping over the surface of the asteroid (shown in translucent white). The field lines are colored by their strength relative to the incoming solar wind values on a log scale (see PDF placeholder image for color bar) from 0.5 (blue) to 10 (red). The field lines were seeded from points evenly spaced along a line across the bottom boundary ($y = -12R_{\text{asteroid}}$, z = 0), as well as points within a sphere of radius $1.2R_{\text{asteroid}}$ centered on the asteroid. This plot corresponds to our denser solar wind case ($T_w = 500 \times 10^3 K$, $\rho_{i,w} = 1000 \text{cm}^{-3}$, $v_w = 500 kms^{-1}$), and a constant $R_M = 5,000$ inside the asteroid.

In Fig. 2 and Table 1 we note that the shell cases for Wind I overshoot the prediction of theoretical maximum from Equation (21), however, this is well within our error bars and not a cause of signficant disagreement between theory and simulation. Future work should explore the parameter space imposed by the shell thickness and conductivity.

4.4 Cometary case

The asteroid body in this case has a resistivity of $2 \times 10^{-3} \eta_c$ or $R_M = 500$, with only the dayside of the 10% shell having $R_M = 5,000$. We ran a simulation for both wind cases. These runs result in higher magnetic field amplification than any of the constant profile cases, but lower than the isotropic shell cases. Physically, this case represents bodies outgassing volatiles from the radiation and incident wind from the host star. ³

Fig. 3, (e) middle right panel and Fig. 5 (b) middle panel show the steady state field configuration for the denser wind run of the comet cases. The cometary case differs from the full shell case in that the field coming in from the back side is smoothly varying (i.e. has no kinks). For the shell case, the field can have a kink at the boundary–allowing higher diffusion inside the body which provides a more uniform field therein. We also reported on this case in O'Brien et al. (2020), Fig. 2 and a video in the supplementary material. This contrasts the 3D model (Fig. 4) of the constant resistivity profile case for $R_M = 5,000$ at the end of §4.2. As in all cases, the peak field is in the zone just outside the boundary on the dayside of the asteroid. Fig.

2 and Table 1 show that the comet case for Wind I (like the shell case above) overshoots the prediction of the theoretical maximum from Equation 21, but this is again well within our error bars and again not a significant disagreement between theory and simulation.

5 INTERPRETATION, APPLICABILITY, AND LIMITATIONS

5.1 Role of solar wind

The ram, thermal, and magnetic energy of the solar wind supply the source of magnetic energy at the dayside boundary of the parent body. If the conductivity of the parent body surface is high enough to sufficiently stall the flow of solar wind, the magnetic field at the boundary keeps increasing until this magnetic pressure can balance the ram, thermal, and magnetic energy of the solar wind. Figure 2 and Table 1 show this trend. Note that the the maximum A in all cases would be better estimated from solving Equation (19) than from the limiting case of Equation (20) but, but for simplicity we discuss the results in terms of how close they approach the simple limit of the latter.

The blue curve, having moderate solar wind parameters of 300cm^{-3} , 5×10^5 K, 100 nT is indeed nearly solar wind limited and the conversion from solar wind pressure to surface magnetic pressure happens relatively efficiently and the value of Equation (20) is approached. The red curve had a higher density, hence the mass loss, and ram pressure terms on the left side of Equation (18) ultimately contribute, lowering the values of the magnetic pressure needed to balance the incoming pressure. Thus the simulated values of A are lower than the red line of $M\sqrt{\gamma\beta}$ from Equation (20) which assumes only magnetic pressure balances the incoming wind pressure. The green curve has a very high β , and hence even lower relative contributions from the magnetic pressure term are needed to balance the incoming pressure and so again slightly lower values achieved than the value of Equation (20).

Current theory and observations of systems analogous to our solar system suggest that the red wind case $(10^3 \text{cm}^{-3}, 5 \times 10^5 \text{ K}, 100 \text{ nT})$ would be closest to the values expected for our sun.

5.2 Effect of numerical resistivity

In Fig. 2, the green-yellow circles show the effect of the imposed numerical diffusion into of our code. The values of the red and blue curves from Equation (21) are ultimately limited by the solar wind. The points on the left region of Fig. 2 ($R_M < 50$) are limited by the magnetic Reynolds number of their true resistivity. However, the resolution of the code introduces a numerical diffusion magnetic Reynolds number ($R_{M\alpha}$) which we defined similarly to R_M in Equation (14).

For the blue and red curves, $R_{M\alpha}$ is a few times higher than the limitation imposed by the stellar wind pressure so we do not see the effect of numerical diffusivity. In contrast, the green wind model has a very high beta (16.66) and high mach number (8.65), i.e. wind parameters are 300 cm⁻³, 1.5×10^5 K, 500 km s⁻¹, 14 nT and so A is thus limited by $R_{M,\alpha}$, as expected from Equation (21). For this case, Fig. 6 shows how the amplification changes with $R_{M,\alpha}$ for 2 different grid resolutions (label shows length of smallest cell). The dip towards the upper right is a numerical artifact of a low resolution grid. This highlights that the grid size chosen must resolve the physics near the surface of the body.

³ Even without the shell, we will show that amplifications > 9 occur *inside* the body, which should be sufficient to explain existing experimental measurements of fields from undifferentiated asteroids. We shall see that the shelled cases allow for even more field pile up. However, when this shell represents an atmosphere, the body beneath could be partially shielded from field pileup in absence of turbulent mixing.

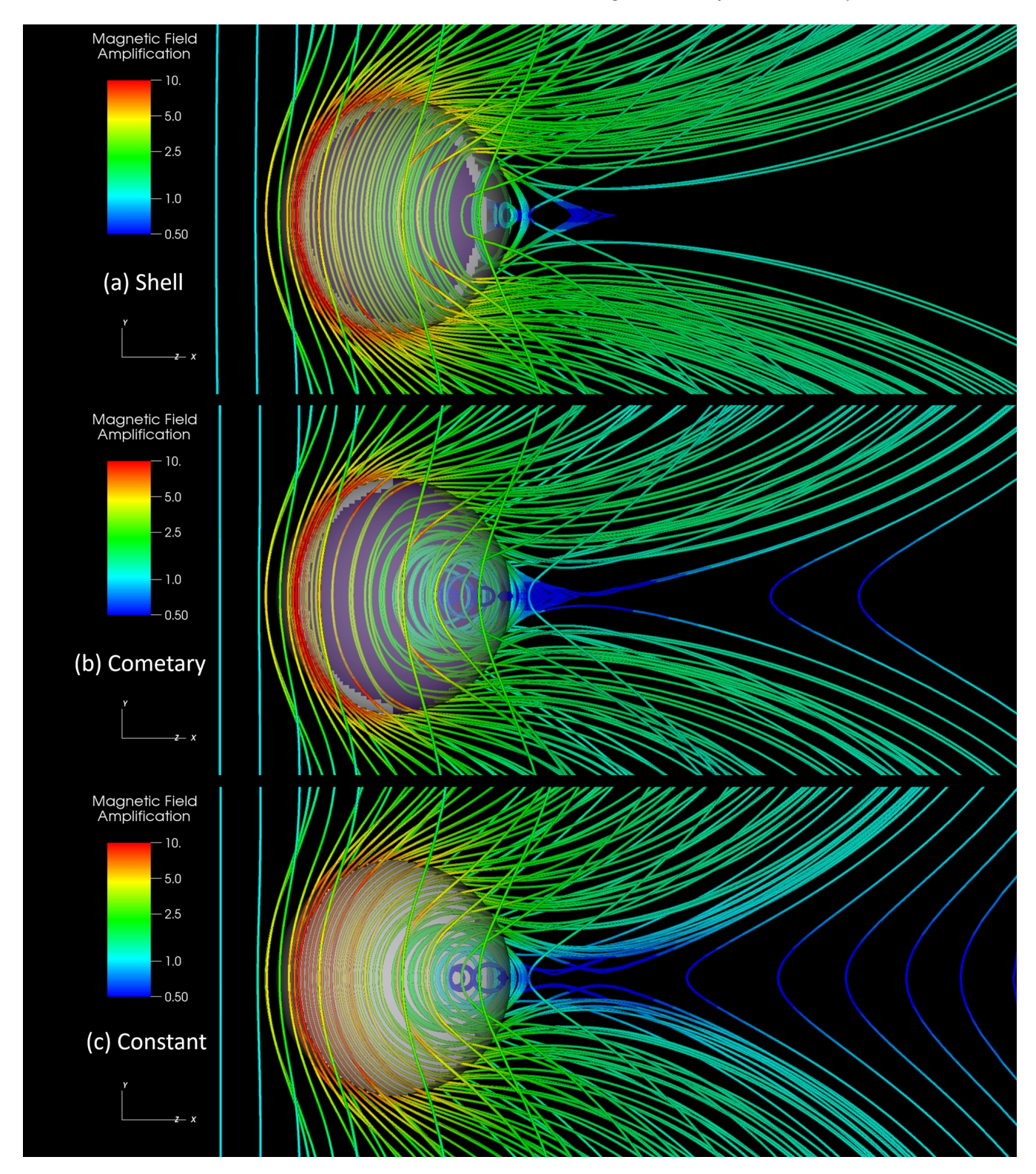


Figure 5. 3D Magnetic Field Structure at quasi-steady state for a subset of cases corresponding to the right column of Fig. 2 at steady state. Shaded violet region in the xy plane inside the body represents a $R_M = 500$, and greyish-white regions $R_M = 5,000$. Cases (a) **Top:** Body with $R_M = 500$, 10% full outer shell $R_M = 5,000$; (b) **Middle**: Body with $R_M = 500$, 10% Cometary dayside shell $R_M = 5,000$; (c) **Bottom**: Constant resistivity profile with $R_M = 5,000$. The strength of amplification increases substantially with the presence of a conducting shell.

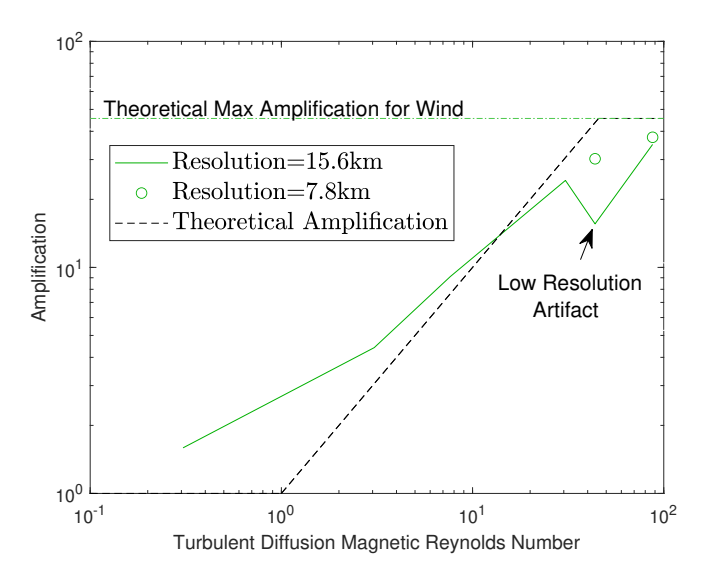


Figure 6. Amplification vs numerical magnetic Reynolds number for the Mach=8.65, Beta=16.66 wind. The horizontal dashed green line shows the value from Equation (20). The rising black dashed lines shows the theoretical prediction for A from Equation (21) which increases with $R_{M\alpha}$ until $R_{M\alpha} > M in(R_M, M\sqrt{\gamma\beta}) = \sqrt{\gamma\beta}$. The solid green line shows the results from simulations for cases with lower resolution, while points show cases with double the resolution to highlight the fact that the dip in the solid green curve is a numerical artifact. Overall, the simulations follow the theoretical trend of the prediction.

5.3 General applicability

The preceding analyses can readily be applied to any asteroid bodies having a constant resistivity profile as seen in Fig. 2. The shell and cometary profiles are applicable to asteroids having a very conductive body. We have only used profiles where the outer 10% shell has 10% the resistivity of the body, but we expect the amplification to hold for thicker shells. For much thinner shells the results may be particularly affected if the shell is so thin that the diffusion time across the shell becomes comparable to or less than the flow crossing time. The result would then be equivalent to a constant profile case with the shell playing little role. If the thicker shells represent atmospheres, then turbulent mixing would be needed for the asteroid body magnetization to gain substantially from the increased pileup. Importantly, the needed pile up to explain some paleofields, as determined by studies of meteorites, is not contingent upon having a shell layer as our constant profile cases have amplifications within 10% of the cometary and shell case values.

In short, our results suggest that apart from the most resistive objects, all bodies considered are able to pile up magnetic fields. The effect is most pronounced for bodies with a conductive shell.

Our WIM can explain why some carbonaceous chondrite meteorites record magnetizations acquired on their parent bodies were undifferentiated. The WIM mechanism may explain other magnetizations from meteorites, and, as exemplified by O'Brien et al. (2020), can in principle be used to constrain the past orbital distance of parent bodies during their magnetization when combined with age information.

In addition, the WIM mechanism may explain magnetizations observed in future space missions to asteroids, such as (16) Psyche, where the nature of the body - in the case of Psyche the origin of its metallic surface - is presently unknown (Elkins-Tanton et al. 2020; Johnson et al. 2020a) and therefore the present/absence of a past core dynamo is similarly undetermined.

5.4 Implications for interpreting previous work

Although the work of O'Brien et al. (2020), supported the possibility originally discussed in Tarduno et al. (2017) that WIM might explain the the magnetization of undifferentiated meteorite parent bodies, Oran et al. (2018) produced a series of magnetohydrodynamic (MHD) simulations that were used to argue that the solar wind was an insufficient source. In fact there is no contradiction between the simulations results in their paper and ours here.

Oran et al. (2018) used a BATS-R-US simulation with a different solar wind model and body resistivity type. While they found amplifications of only about 3, this is perfectly in line with the maximum amplification that our theory predicts for a $35 \, \mathrm{cm}^{-3}$, $700 \, \mathrm{km} \, \mathrm{s}^{-1}$, $50,000 \, \mathrm{K}$ solar wind used in their simulations. In fact we ran a case using exactly their wind model and resistivity and found a steady state amplification values equal to their to within a few percent. This verifies that both simulation methods are mutually consistent and that there is no contradiction between their computation and ours. However, we have also shown more generally how higher amplifications are possible with different sets of parameters that are realistic for the early solar wind.

5.5 Limitations and approximations

Here we comment on how some of the limitations and approximations affect the results:

- Cartesian Grid: AstroBEAR currently does not have an option for running simulations in spherical coordinates. Hence, there are small "staircase" like artifacts on the surface of the asteroid in our models. These features decrease with resolution (or AMR level used), but the tiny increase in accuracy was not worth the increase in memory and core hours. For cases with low resistivity, some cells on the dayside oversaturated with magnetic field, causing small time steps and slowing the simulation to a halt. We circumvented this problem by using a controlled numerical diffusivity, characterized by our $R_{M_{\alpha}}$, for all flows outside the asteroid. This sped up the steady state convergence efficiently, with 256 core hours being sufficient for low to moderate resistivity.
- Rarefactions on the Night Side: As Fig. 3 shows, the night side of the asteroid has the lowest densities in the plot region. In several cases this required use of AstroBEAR's minimum density protections to avoid the extremely high velocites that would otherwise cause the time steps to catastrophically decrease and halt the simulation.

Several other approximations warrant mention:

- Size of Parent Body: We have taken the size to be 500 km. Our use of an MHD code is necessarily incomplete given that the wind is really a collisionless plasma, but the approximation is not unreasonable as long as the body size is much larger than the gyroradius of the ions.
- **Revolution of the Asteroid:** We calculated the axial component of the Tidal force $(a_{t, \text{axial}} \sim \Delta r G M_{\odot}/R^3 \sim 5 \text{nm s}^{-2})$, and the Coriolis Force $(a_c = 2\Omega \times v' \sim 1.48 \text{mm s}^{-2})$ assuming the asteroid to be at 2 AU, and found that these can be neglected. Hence, we do not benefit from using a frame of reference co-rotating with the asteroid.
- Magnetic permeability of Asteroids: Here we have not accounted for the magnetic permeability of the asteroids. We expect it to be the same order of magnitude as vacuum, but including it could increase the field strength actually experienced by the body by $\gtrsim 10\%$ depending on the material.

6 CONCLUSION

From computational simulations and theoretical analyses, we have shown that magnetic flux pile up from an impinging stellar wind can substantially magnetized an otherwise unmagnetized asteroid. As applied to the early solar wind, which would would have had a higher ram pressure than that of the present day, we find that the ambient solar find field can be amplified by factors A > 9 even without a shell of enhanced conductivity above that of the main body. This may explain natural remanent magnetization (NRM) found in undifferentiated solar system bodies. With a conductive shell layer surrounding a parent body, we find that even larger amplification factors A > 10 in this shell layer is very much possible for early solar wind properties well within theoretical model limits and observational constraints.

The solar wind properties, and the effective resistivity of the asteroid's shell layer emerge as the two most important factors affecting the amount of magnetic field pileup.

The WIM mechansim and the predicted amplification scaling are quite general, and can be applied to any magnetized stellar wind and asteroid combination. The WIM mechanism is also potentially important to explain magnetizations of asteroids measured from future space missions such as (16) Psyche. The results would ultimately be applicable to extrasolar planetary systems as well.

Finally, we note there are important microphysical aspects of the wind-asteroid interaction that we have not included, and warrant higher fidelity modeling the future. At the MHD level this could include anisotropic viscosity due to the magnetic field which may be important at the wind-asteroid interface. If our shell cases were interpreted to model bodies with atmospheres, they should ultimately be augmented to include atmospheric flows which could lead to mixing within the atmosphere and/or between the atmosphere and surface layer. This will be important for determining how much of the piled up field at the top of an atmosphere could reach the solid surface layers. In addition, the microphysics of how the field is separated from plasma and deposited into solid asteroid material at the interface is not directly treated in the MHD approximation and could benefit from computational models that that follow particles below at ion-gyroradii scales and/or have plasma-solid interaction capability. There is substantial opportunity for further work in all of these directions.

ACKNOWLEDGEMENTS

AA acknowledges a Horton Graduate Fellowship from the UR Laboratory for Laser Energetics. The authors thank the Center for Integrated Research Computing (CIRC) at the University of Rochester for providing computational resources and technical support. Support provided from grants NSF PHY-2020249, NASA grant 80NSSC19K0510, NSF EAR-2051550.

REFERENCES

- Blackman E. G., Owen J. E., 2016, Monthly Notices of the Royal Astronomical Society, 458, 1548
- Bono R. K., Tarduno J. A., Nimmo F., Cottrell R. D., 2019, Nature Geoscience, 12, 143
- Brownlee D., 2005, in Davis A., ed., No. v. 1, Meteorites, Comets, and Planets: Treatise on Geochemistry, Second Edition, Volume 1. Elsevier Science, Chapt. 125, pp 663–737, https://books.google.com/books?id=kYtksEUxw0oC
- Bryson J. F., Church N. S., Kasama T., Harrison R. J., 2014a, Earth and Planetary Science Letters, 388, 237

- Bryson J. F., Herrero-Albillos J., Kronast F., Ghidini M., Redfern S. A., van der Laan G., Harrison R. J., 2014b, Earth and Planetary Science Letters, 396, 125
- Carporzen L., Weiss B. P., Elkins-Tanton L. T., Shuster D. L., Ebel D., Gattacceca J., 2011, Proceedings of the National Academy of Sciences, 108, 6386
- Carroll-Nellenback J. J., Shroyer B., Frank A., Ding C., 2013, Journal of Computational Physics, 236, 461
- Collinson D. W., Hide R., Hutchison R., Runcorn S. K., 1994, Philosophical Transactions: Physical Sciences and Engineering, 349, 197
- Cunningham A. J., Frank A., Varnière P., Mitran S., Jones T. W., 2009, ApJS, 182, 519
- Duba A., Boland J., 1984, Lunar planet. Sci., 15, 232
- Elkins-Tanton L. T., Weiss B. P., Zuber M. T., 2011, Earth and Planetary Science Letters, 305, 1
- Elkins-Tanton L. T., et al., 2020, Journal of Geophysical Research (Planets), 125, e06296
- Jia X., Slavin J. A., Gombosi T. I., Daldorff L. K. S., Toth G., van der Holst B., 2015, Journal of Geophysical Research: Space Physics, 120, 4763
- Johnson C. L., et al., 2015, Science, 348, 892
- Johnson B. C., Sori M. M., Evans A. J., 2020a, Nature Astronomy, 4, 41
- Johnson C. L., et al., 2020b, Nature Geoscience, 13, 199
- Johnstone C., Güdel M., Brott I., Luftinger T., 2015, Astronomy & Astrophysics, 577
- Nagashima K., Krot A. N., Komatsu M., 2017, Geochimica et Cosmochimica Acta, 201, 303
- Nagashima K., Kita N. T., Luu T.-H., 2018, 26Al–26Mg Systematics of Chondrules. Cambridge University Press, p. 247–275, doi:10.1017/9781108284073.009
- Nagata T., 1979, Physics of the Earth and Planetary Interiors, 20, 324
- O'Brien T. M., Tarduno J. A., 2016, in Lunar and Planetary Science Conference. Lunar and Planetary Science Conference. p. 2913
- Oran R., Weiss B. P., Cohen O., 2018, Earth and Planetary Science Letters, 492, 222
- O'Brien T., Tarduno J. A., Anand A., Smirnov A. V., Blackman E. G., Carroll-Nellenback J., Krot A. N., 2020, Nature Communications Earth & Environment
- Scott E. R. D., Krot A. N., 2014, Chondrites and Their Components. pp 65--137
- Tarduno J. A., et al., 2012, Science, 338, 939
- Tarduno J. A., Blackman E. G., Mamajek E. E., 2014, Physics of the Earth and Planetary Interiors, 233, 68
- Tarduno J. A., Cottrell R. D., Davis W. J., Nimmo F., Bono R. K., 2015, Science, 349, 521
- Tarduno J. A., O'Brien T. M., Smirnov A. V., 2016, in Lunar and Planetary Science Conference. Lunar and Planetary Science Conference. p. 2609
- Tarduno J. A., O'Brien T. M., Blackman E. G., Smirnov A. V., 2017, in Lunar and Planetary Science Conference. Lunar and Planetary Science Conference. p. 2850
- Tarduno J. A., et al., 2020, Proceedings of the National Academy of Sciences, 117, 2309
- Weiss B. P., Elkins-Tanton L. T., 2013, Annual Review of Earth and Planetary Sciences, 41, 529
- Wood B. E., Müller H. R., Zank G. P., Linsky J. L., Redfield S., 2005, ApJ, 628, L143

This paper has been typeset from a $T_EX/I \triangle T_EX$ file prepared by the author.